THE JOURNAL OF PHYSICAL CHEMISTRY A
A JOURNAL OF THE AMERICAN CHEMICAL SOCIETY

pubs.acs.org/JPCA Article

From Incident Light to Persistent and Regenerable Radicals of Urea-Assembled Benzophenone Frameworks: A Structural Investigation

Dustin W. Goodlett, Ammon J. Sindt, Muhammad Saddam Hossain, Rajkumar Merugu, Mark D. Smith, Sophya Garashchuk, Anna D. Gudmundsdottir, and Linda S. Shimizu*

Cite This: *J. Phys. Chem. A* 2021, 125, 1336–1344 Read Online

ACCESS | Metrics & More | Article Recommendations | Supporting Information

ABSTRACT: Herein we probe the effects of crystalline structure and geometry on benzophenone photophysics, self-quenching, and the regenerable formation of persistent triplet radical pairs at room temperature. Radical pairs are not observed in solution but appear via an emergent pathway within the solid-state assembly. Single crystal X-ray diffraction (SC-XRD) of two sets of constitutional isomers, benzophenone *bis*-urea macrocycles, and methylene urea-tethered dibenzophenones are compared. Upon irradiation with 365 nm light-emitting diodes (LEDs), each forms photogenerated radicals as monitored by electron paramagnetic resonance (EPR). Once generated, the radicals exhibit half-lives from 2 to 60 days before returning to starting material without degradation. Re-exposure to light regenerates the radicals with similar efficiency. Subtle differences in the structure of the crystalline frameworks modulates the maximum concentration of photogenerated radicals, phosphorescence quantum efficiency (φ), and n-type self-quenching as observed using laser flash photolysis (LFP). These studies along with the electronic structure analysis based on the time-dependent density functional theory (TD-DFT) suggest the microenvironment surrounding benzophenone largely dictates the favorability of self-quenching or radical formation and affords insights into structure/function correlations. Advances in understanding how structure determines the excited state pathway solid-state materials undertake will aid in the design of new radical initiators, components of OLEDs, and NMR polarizing agents.

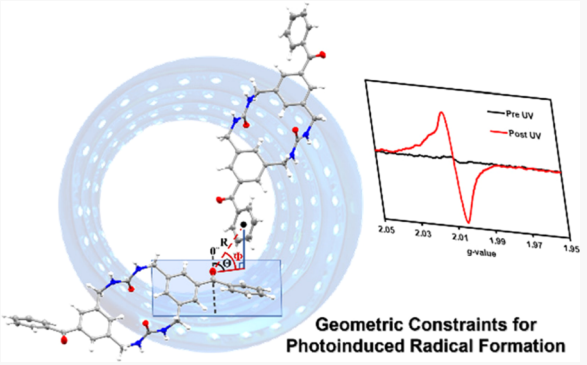

1. INTRODUCTION

The supramolecular assembly of chromophores provides an alternative approach to modulate photophysics and afford functional hierarchical materials.[1−3] Self-assembly often leads to dramatic changes in photophysics,[4] formation of porous materials,[5,6] and can result in the emergence of new properties such as persistent radical formation.[7,8] Recently, our group reported that self-assembled benzophenones **2**−**4** (Figure 1) exhibit persistent radical formation upon irradiation with UV light when in the solid-state but show no radicals in solution.[9] Here, we examine how solid-state assembly of two benzophenone (BP) *bis*-urea macrocycles and two methylene-urea tethered dibenzophenones **1**−**4** influences the rate of radical formation, maximum quantity of radicals, and radical regeneration. The macrocycles differ in the position of the BP groups on the exterior of **1** and within the macrocycle of **4**. The linear analogs differ in attachment location *meta* or *para* with respect to the methylene-urea group. These materials were also examined by laser flash photolysis (LFP) in nanocrystalline suspensions to probe their excited states. Subtle changes in the microenvironments of the BPs govern processes accessible from its excited state including radical formation, phosphorescence quantum efficiency (φ), self-quenching and other types of non-radiative decay.

BP is an efficient triplet sensitizer that rapidly undergoes intersystem crossing from an S_1 to T_2 and ultimately T_1 state.[10] From the T_1 state, BP can undergo phosphorescence,[10] non-radiative decay,[11] intermolecular energy transfer, or abstraction of a neighboring hydrogen to form a ketyl radical,[12] which commonly leads to dimerization.[13,14] Early studies of triplet-triplet energy transfer in mixed BP/naphthalene glasses displayed phosphorescence of naphthalene after BP excitation.[15] Later, triplet excited BP (^{3}BP) was shown to undergo electron transfer with neighboring BPs via π-type or n-type self-quenching mechanisms.[16,17] The π-type self-quenching occurs when the lone electron in the π^* orbital of ^{3}BP is donated to the empty π^* orbital of a neighboring ground state BP. In contrast, n-type self-quenching occurs by donation of an

Received: October 1, 2020
Revised: January 20, 2021
Published: February 3, 2021

https://dx.doi.org/10.1021/acs.jpca.0c08953
J. Phys. Chem. A 2021, 125, 1336−1344

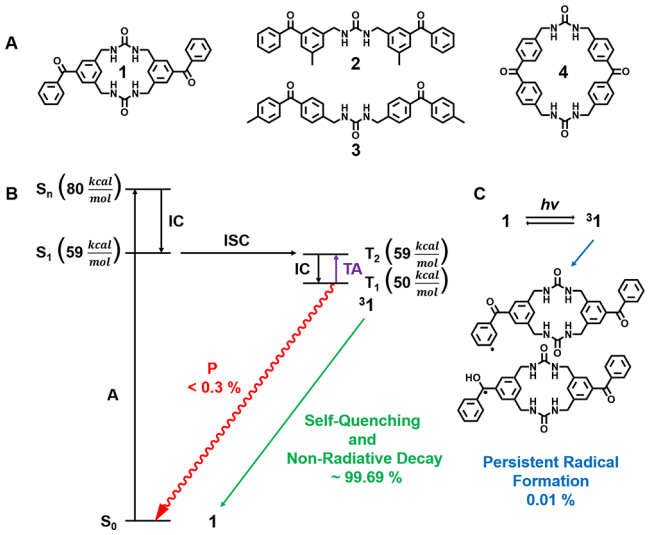

Figure 1. (A) Comparison of BP structures **1**−**4**. (B) Solid-state assembly influences the Jablonski diagram for **1.** The triplet excited state can undergo at least three competing processes, i.e. phosphorescence (P), self-quenching, and persistent radical formation. A = absorbance, IC = internal conversion, ISC = intersystem crossing, TA = transient absorption. Energies were calculated for a single molecule of **1** by TD-DFT using the ωB97XD/6−31 + G** level of theory. S_n estimated from the strongest transition near λ_{exc} = 365 nm. (C) Hypothesis for triplet radical pair formation upon irradiation in the solid-state.

electron from the aryl ring of a ground state BP to the electron deficient lone pair orbital of the oxygen of a neighboring ^{3}BP. Correlation of geometric parameters from X-ray structures with photochemical reactions was pioneered by Schmidt[18] and Scheffer.[19] The Garcia-Garibay group showed that nanocrystalline suspensions of BP favor n-type self-quenching with more electron rich BPs displaying faster rates of self-quenching. These studies defined three geometric considerations that modulate n-type self-quenching including (1) the distance (R) between BP* oxygen to the centroid of a nearby aryl ring, (2) the azimuth (Θ) angle which is defined as the angle between the oxygen atom of BP* and the projection of R, and (3) the altitude (Φ) angle which is defined as the angle between the plane in which the ketone of BP* resides and the centroid of the nearby aryl ring.[17] Assembled systems from our group enable us to probe these geometric influences and evaluate the importance of these constraints.

We have employed urea guided self-assembly to control the environment around the BP. This organization provided a reaction pathway from the excited state that is not typically observed in solution.[9] Assembled BP macrocycle **4** exhibited photo-induced persistent radical formation whereas no radicals are detected in solution.[7] These radicals persisted for weeks at room temperature and were used as polarizing agents for magic angle spinning dynamic nuclear polarization NMR enhancement.[7] High field and X-band EPR studies both suggested two delocalized radicals. Our hypothesis is that these are ground state triplet radical pairs.[7] The pathway to radical formation was not unique to **4**, as linear analogs **2** and **3** also exhibited persistent radicals upon UV irradiation in the solid-state.[9]

In this work, we report the structure of **1**, compare assembled BP structures of **1**−**4**, assess abstractable hydrogens, and evaluate geometric conditions for self-quenching. Experimental measurements of phosphorescence quantum efficiency (φ) and efficiency of radical pair generation are compared with ideal geometric values for n-type self-quenching. Finally, excited intermediates upon excitation of **1**, **3** and **4** were directly observed using LFP and were examined by time-dependent density functional theory (TD-DFT) calculations. This combined data presents detailed insight into how navigation through excited state pathways is influenced by the material's structure.

2. EXPERIMENTAL AND COMPUTATIONAL DETAILS

2.1. Synthesis and Characterization of Compounds. Compounds **1**−**4** were synthesized as previously described.[9,20] Macrocycle **1** is sparingly soluble in hot DMSO and DMF; and only recently gave single crystals of suitable size for SC-XRD data collection. The final products were triply recrystallized to ensure purity for EPR, LFP, and photophysical studies. Studies below were carried out on bulk freshly crystallized samples of **1**−**4**. All commercial reagents and solvents were purchased from Alfa Aesar, Sigma-Aldrich, VWR, or TCI America and were used as received without further purification. ^{1}H-NMR data were collected using Bruker Avance III-HD spectrometers (300−400 MHz). Chemical shifts are reported as (δ ppm) along with the corresponding integration values. Coupling constants (J-values) are reported in hertz (Hz).

2.2. Crystallization of Compounds. Slow evaporation of macrocycle **1** in DMSO (5 mg/mL) at 125 °C for ∼5 h afforded needle-like crystals (0.3 x 0.04 x 0.02 mm^3) of $C_{32}H_{28}N_4O_4$ in the monoclinic system with the $P2_1/n$ space group. Compounds **2** ($C_{31}H_{28}N_2O_3$) ($P2_1$) and **3** ($C_{31}H_{28}N_2O_3$) ($P1$ (no. 1)) as well as the solvate **4** ($C_{32}H_{26}N_4O_4{\cdot}(CH_3)_2SO$) ($P2_1/c$) were crystallized as previously reported.[9,16] Reported structures: **2** CCDC No. 1855193, **3** CCDC No. 1855192, **4** CCDC No. 1534513.

2.3. X-Ray Structure Determination. X-ray intensity data from a colorless needle of **1** were collected at 100(2) K using a Bruker D8 QUEST diffractometer equipped with a PHOTON-100 CMOS area detector and an Incoatec microfocus source (Mo Kα radiation, λ = 0.71073 Å). The raw area detector data frames were reduced and corrected for absorption effects using the Bruker APEX3, SAINT+ and SADABS programs.[22,23] The structure was solved with SHELXT.[24] Subsequent difference Fourier calculations and full-matrix least-squares refinement against F^2 were performed with SHELXL-2018[25] using OLEX2.[26]

2.4. Solid-State Photophysical Properties. Diffuse reflectance spectra were recorded on crystals of **1** pre/post exposure to 365 nm LEDs using a Perkin Elmer Lambda 45 UV/vis spectrometer with a reliable range of 280−1100 nm equipped with UV Winlab software and were referenced to Spectralon. Emission analysis was performed using a Perkin Elmer LS 55 fluorescence spectrometer with a range of 200−900 nm equipped with a pulsed high-energy source for excitation (Front-Face mode). The phosphorescence quantum efficiency (φ) measurements were collected on an Edinburgh FS5 fluorescence spectrometer equipped with a 150 W Continuous Wave Xenon Lamp source for excitation (SC-30: Integration Sphere module).

2.5. Laser Flash Photolysis (LFP) Measurements. Crystals of **1**, **3**, and **4** were ground using a mortar and pestle, and subsequently suspended in water. The suspensions were sonicated for 4 min, then let stand for 2 min; and this process was repeated 3 times.[17] The resulting mixtures were transferred into quartz cuvettes and degassed with either argon or oxygen.

https://dx.doi.org/10.1021/acs.jpca.0c08953
J. Phys. Chem. A 2021, 125, 1336−1344

A fresh suspension was prepared for each LFP measurement. The excitation wavelength for all the LFP experiments was 266 nm. Detailed description of the setup has been reported.[27]

2.6. UV Irradiation. Freshly recrystallized material was filtered and dried under Ar (g) at room temperature and placed in quartz EPR tubes. The tubes were oriented horizontally in the photoreactor containing Waveform Lighting real UV LED strips (365 nm, 4.5 W/ft., 3.2 ft., Figure S51).

2.7. Electron Paramagnetic Resonance (EPR) Measurements. EPR data was collected using a Bruker EMX plus equipped with a Bruker X-band microwave bridgehead and Xenon software (v 1.1b.66). The spectra were doubly integrated using the Xenon software and the resulting areas were converted to ppm using a TEMPO calibration curve (Figure S36). Samples were sealed under Ar in Norell Suprasil Quartz EPR tubes before exposure to the 365 nm LEDs.

2.8. Simulation of Diffuse Reflectance and Absorbance Measurements. Gas phase TD-DFT calculations using geometries from SC-XRD data were performed with the ωB97XD/6−31+G** level of theory[9] to simulate the experimental diffuse reflectance measurements for macrocycles **1** and **4**. Their absorbance was also simulated in solution within the polarized continuum model.[27] The geometry of both materials was optimized using the same level of theory with the dielectric constant set to that of DMSO (47.24). All electronic structure calculations were performed with Q-Chem 5.2 quantum chemistry software [QCHEM].[29] 25 excited states were used to generate spectra using geometry of a single molecule from the X-ray structure and 15 states for minimized geometry in solution. Natural transition orbitals (NTOs) were visualized using IQmol v2.14.0. Charge transfer descriptors and electron/hole population analysis were determined using the TheoDORE software package (http://theodore-qc.sourceforge.net/).[30] Additionally, the employed method was tested against LRC-wPBEh/6−31+G** and B3LYP/6−31+G** for single molecules and a pair of neighboring molecules using the geometry from the SC-XRD data for 1 (Figures S52−54). The theoretical spectra are generated from the excited state energies and oscillator strengths by assuming the Gaussian band shape for each peak and summing over the excited states, labeled by the index n according to the following expression:

$$g(x) = \sqrt{\frac{1}{\pi\sigma^2}} \sum_{n} f_n \, e^{-(x-x_n)^2/\sigma^2} \quad (1)$$

In eq 1 x is the energy variable expressed in nm, x_n is the position of the nth line (in nm), and f_n is the corresponding oscillator strength. The parameter σ is the 'standard deviation' controlling the width of the Gaussian; its value is set to 25 nm throughout this work.

2.9. Simulation of Transient Absorption from LFP Measurements. Partial gas phase geometry optimizations on the atomic coordinates from SC-XRD data of **1**, **3**, and **4** were carried out using the ωB97XD/6−31+G** level of theory. All atoms were space fixed except the C═O of ^{3}BP and the atoms at the radical site for the optimizations on the triplet excited and proposed radical species respectively (Figure 4A,C,D). TD-DFT calculations using the same level of theory were then carried out on the optimized structures.

3. RESULTS AND DISCUSSION

3.1. Directed Assembly to Control the Organization of BP within Crystalline Frameworks. Compounds **1**−**4** utilize the urea hydrogen bonding motif to direct their assembly, effectively controlling the organization of BP in the solid-state. This enables us to investigate the geometric rules explored by the Garcia-Garibay group for self-quenching versus hydrogen abstraction using two sets of constitutional isomers. New to this work is **1**, which positions the BPs on the exterior of a smaller xylene macrocycle. The X-ray structure revealed the desired macrocycle in the monoclinic system with the $P2_1/n$ space group. The urea adopts a typical *trans-trans* conformation assembling into cylinders (Figure 2A) with no

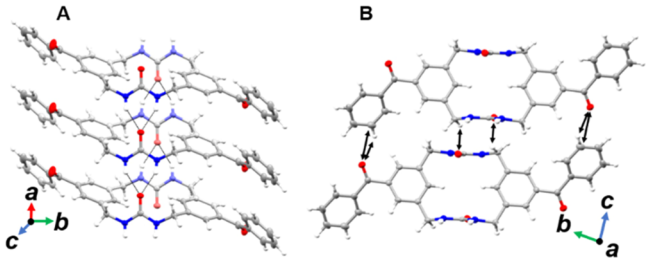

Figure 2. (A) Three-centered urea hydrogen bond driven assembly of **1** into cylinders. (B) View along the *a*-axis displaying short contacts between two macrocycles.

interior cavity through the characteristic three-centered urea hydrogen bond (d(N···O) = 2.829(2) and 2.888(3) Å) along the *a*-axis. On each side of the columns a phenyl and carbonyl group of the BP project outward with their two carbonyls oppositely oriented (Figure 2B). The cylinders pack together to form herringbone[31] arrays as depicted in Figure S5C. Short contacts, which are less than the sum of the *van der Waals* radii are shown between two neighboring columns in Figure 2B and these interactions are repeated infinitely along the *c*-axis.

For comparison, macrocycle **4** crystallizes as colorless needles in the monoclinic system in the $P2_1/c$ space group.[16] The larger dimensions of this spacer define an interior pore, which is filled with DMSO (Figure 3A and Figure S6).[16] The tubes form along the crystallographic *a*-axis and are held together by the urea hydrogen bonding motif (range d(N···O) = 2.963(5) - 3.082(5) Å, Figure 3A). Individual columns pack hexagonally, which stagger the BP units along the *c*-axis. Heating to 100 °C does not remove the DMSO guests, higher temperature or vacuum is required. Measurements on this system were carried out on the stable DMSO inclusion complex.

Linear analogue **2** has a *meta* relationship between the BP carbonyl and the methylene urea and crystallizes in the acentric $P2_1$ space group. The molecule adopts a C-shape that organizes the two BPs in close proximity (Figure 3B,C). Slightly shorter urea hydrogen bonding interactions (d(N···O) = 2.800(6) and 2.809(6) Å) organize the BP groups down the *a*-axis. In comparison, analogue **3** crystallizes in the acentric space group *P*1 (no. 1).[9] The urea groups adopt a *trans-trans* conformation and three centered hydrogen bonding (d(N···O) = 2.899(5) and 2.962(4) Å) direct the formation of tapes (Figure 3D). The BP units are stretched linearly outward from the urea group with their carbonyl groups oppositely oriented.

Our working hypothesis is that BP photophysics follows expected pathways with rapid ISC from $S_1 \rightarrow T_2 \rightarrow T_1$. LFP

https://dx.doi.org/10.1021/acs.jpca.0c08953
J. Phys. Chem. A 2021, 125, 1336−1344

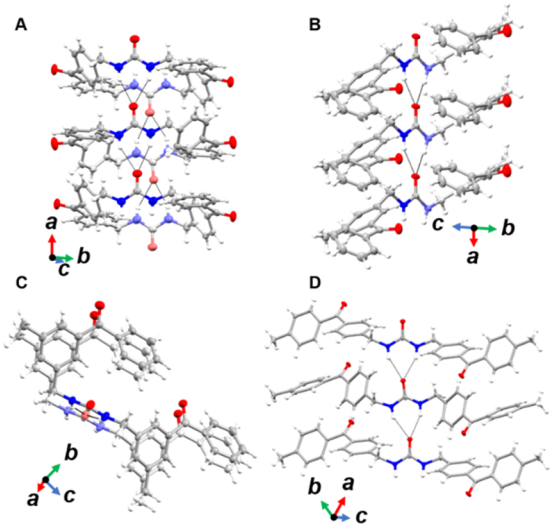

Figure 3. (A) Infinite tubes created by urea hydrogen bond driven assembly of **4** (DMSO molecules within the pore have been omitted for clarity). (B) Bifurcated urea hydrogen bond directed assembly of **2**. (C) Alternate view of **2** down the *a*-axis highlights the molecule's adoption of a C-shape. (D) Urea driven assembly of **3** with a linear conformation.

experiments herein, enable us to further probe this pathway. In the crystals, the ^{3}BP can abstract a neighboring hydrogen to give triplet radical pairs that do not dimerize (Figure 1C).[7] These radicals appear to persist until they undergo the reverse process.[7] Alternatively, radical pairs could be generated by cleavage about the BP ketone's alpha carbon.[32] The bond dissociation energy (BDE) for the alpha carbon of BP has been reported as low as 90.1 kcal/mol.[33] In the solid-state, these radicals may recombine as no degradation products were observed.

Figure 4 compares the hydrogens within 3.13 Å of the BP* oxygen atom for **1**−**4**, which is the furthest distance reported for intermolecular H-abstraction by BP.[34,35] To estimate the bond dissociation energies (BDEs), the ALFABET machine learning tool was employed.[36] Inspection of **1** and **3** reveals that only aryl hydrogens are available for abstraction within this range (Figure 4A,C). ALFABET approximates the BDEs for the *m*-aryl hydrogen of **1** to be 111.4 kcal/mol and the *o*-aryl hydrogen of **3** to be 109.1 kcal/mol. In comparison, **2** (Figure 4B) has four types of H's in proximity to a neighboring BP* oxygen (methyl: 90.1 kcal/mol BDE, methylene: 79.9 kcal/mol BDE, *m*-aryl: 111.4 kcal/mol BDE, and *p*-aryl: 111.2 kcal/mol BDE). The methyl and methylene BDEs from ALFABET are consistent with the literature which reports a benzylic hydrogen BDE value of ∼88 kcal/mol.[33] Macrocycle **4** shows aryl and benzyl protons with the benzyl H's closer in proximity (2.4 vs 2. 8 Å, Figure 4D). The BDE of the benzyl and aryl hydrogens were estimated as 77.3 and 111.5 kcal/mol respectively. Photo-oxidation reactions in benzene solution with **4** demonstrate that its ketyl radical may abstract a hydrogen atom from benzene (BDE ∼111 kcal/mol)[33] as significant amounts of biphenyl were observed, suggesting that the assembled ketyl radical is quite reactive.[6] Unsubstituted BP is also capable of hydrogen abstraction from benzene.[37]

Possible pathways open to ^{3}BP include self-quenching (π or n-type), other non-radiative processes, phosphorescence, and H-abstraction. For simplicity, the ring nearest the BP* oxygen (R in Å, Figure 4E) is labeled as α and the other is β. The

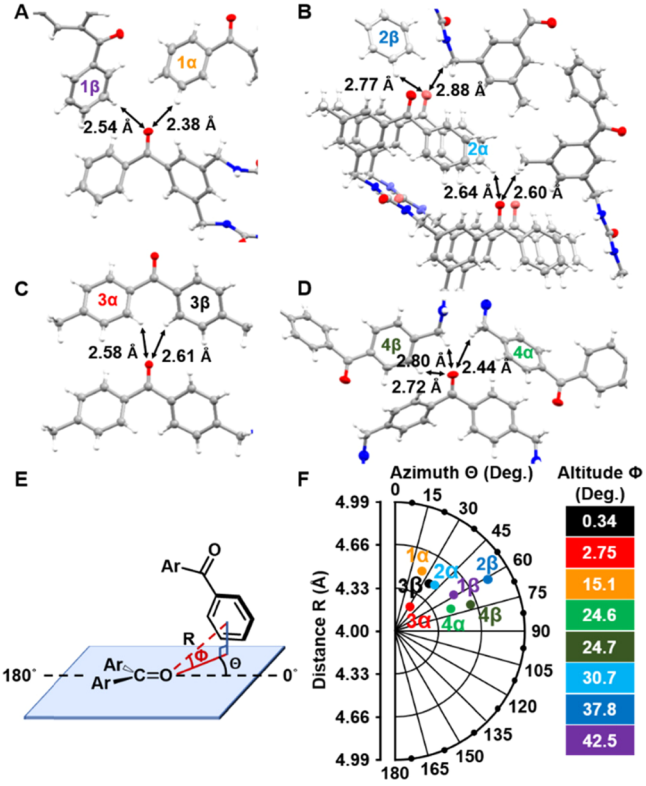

Figure 4. Detailed analysis of SC-XRD data for **1**−**4**. (A−D) Display of the hydrogen atoms within 3.13 Å from a neighboring BP carbonyl oxygen atom. The aromatic rings are labeled either α for the nearest BP ring or β. (E) Geometric considerations for n-type self-quenching including the distance (R), azimuth (Θ), and altitude (Φ) angles. (F) Three-dimensional polar contour plot displaying values for Θ, Φ, and R for α and β aromatic rings of **1**−**4**.[17]

optimized geometry for π-type quenching places a BP aryl ring parallel to the ketone of BP*. However, analysis of the assembled structures of **1**−**4** shows that no BP rings (α or β) have the required geometry for π-type quenching. In n-type quenching, the aryl ring should be orthogonal to the oxygen atom of BP* with the optimal distance R within van der Waals contact, azimuth angle Θ between 60−90°, and the altitude angle Φ closest to 0° (Figure 4E).[17] Three of the assemblies show favorable Θ values while in **3** the Θ is unfavorable (35.0°, 38.2°, Table S15). However, **3** does have favorable Φ values (2.75°, 0.34°, Figure 4F). Here, we test the influence of geometric traits on diffuse reflectance, quenching of phosphorescence, LFP, and photogenerated radical measurements.

3.2. Solid-State Absorption and Emission Spectra. In DMSO solution, these materials exhibit similar absorption spectra with a strong $\pi\,\pi^*$ band at λ_{max} = ∼260 nm and a weak n π^* band at λ_{max} ∼340 nm, similar to other BPs.[9,21] The $\pi\,\pi^*$ band is shifted significantly in assembled **1**−**4**, appearing as a broad absorption between λ_{max} = 355−382 nm (Figure S7A).[7,9] The diffuse reflectance correlates with the torsional angle between the two aryl rings of the BP when comparing each set of constitutional isomers. Macrocycle **1** (22.5°) has a higher λ_{max} (366 nm) than macrocycle **4** (55.2°) with λ_{max} = 355 nm (Figure S13). Linear analog **3** (29.3°) also shows a higher λ_{max} = 382 nm than **2** (44.5°) λ_{max} = 374 nm (Figure S14).

https://dx.doi.org/10.1021/acs.jpca.0c08953
J. Phys. Chem. A 2021, 125, 1336−1344

The emission spectra of **1**−**4** in solution (DMSO, 0.9−1.0 mM, λ_{ex} = 340 nm) showed broad transitions from λ_{em} = 435−502 nm.[7,9] Assembly causes an overall shift with λ_{em} = 480−528 nm. The phosphorescence lifetimes are quite short (τ = 1.5−2 ns) in solution and are slightly quenched upon solid-state assembly ranging from τ = 0.32−1.3 ns.[9,21] Phosphorescence quantum efficiencies are below the limits of detection (φ = < 0.3) for all materials in solution but is slightly increased in assemblies of both **1** and **3** (φ = 1.55, 5.0).[9]

3.3. TD-DFT Simulations of Diffuse Reflectance Data. To characterize the excited state transitions of **1** and **4**, the diffuse reflectance spectra were calculated using a similar approach as employed for **2** and **3**.[9] TD-DFT calculations were performed in the gas phase with geometries from SC-XRD data at the ωB97XD/6−31+G** level of theory. The resulting spectral lines were used to simulate the experimental diffuse reflectance measurements for both macrocycles. The theoretical spectra for **1** and **4** were scaled by multiplying the calculated energies (in eV) by 0.667 and plotted versus the experimental spectra in Figures S8A and S10A. The computed spectra were generated according to eq 1 for sigma = 25 nm and give the same shape with similar relative energies as the experimental data, which validates the theoretical method. The absorbance of both macrocycles was also simulated in solution using geometries optimized with the polarized continuum model in DMSO (Figures S9 and S11).[28]

The simulated natural transition orbitals (NTOs) for the π π^* transitions for **1** in solid-state are quite similar to those in solution (Figures S8B and S9D). Inspection of occupied NTO 4 shows electron density delocalized across both BPs and methylene-urea bridges in the solid-state. In contrast, the virtual orbitals show no contributions from the bridges. Macrocycle **4** exhibits quite different NTOs in the solid-state. Here, the occupied NTO 6 shows electron density primarily on one of the aromatic rings of the BP units. The virtual orbitals are slightly more delocalized across the BPs. In solution, the occupied NTO 4 is delocalized across one BP unit and the two bridges. A similar trend is seen in the virtual orbitals. The spatial overlap among the frontier orbitals of both materials suggests that there is no charge transfer between different parts of the molecule, which correlates well with TheoDORE calculations (Tables S8−S11).

3.4. LFP Experiments. The transient spectra of nanocrystalline argon- and oxygen-saturated water suspension of macrocycles **1**, **4**, and linear analog **3** were obtained with ICCD camera from 300 to 750 nm. The normalized spectra of **1** has a broad absorption between 450 and 750 nm, with the kinetic profile being the same across the spectrum. The transient absorption is formed faster than the time resolution of the laser flash system and the decay of the absorption can be fit as a mono-exponential function with a rate constant of 1.4 × 10^7 s^{-1}, there is a longer-lived residual absorption, but it is too weak to be fitted accurately. In oxygen-saturated solution, the lifetime is not affected significantly but the yields of the absorption are slightly reduced.

The transient spectrum of **3** also resulted in a broad transient absorption between 450 and 750 nm with maximum absorption around ∼650 nm. In argon-saturated suspension the decay of the signal was fitted as a mono-exponential decay resulting in a lifetime of 51 ns, with a weak residual absorption. In oxygen saturated suspension the rate of decay was not affected significantly but the yields were reduced. In comparison, the transient spectrum of **4** (Figure 5A) showed

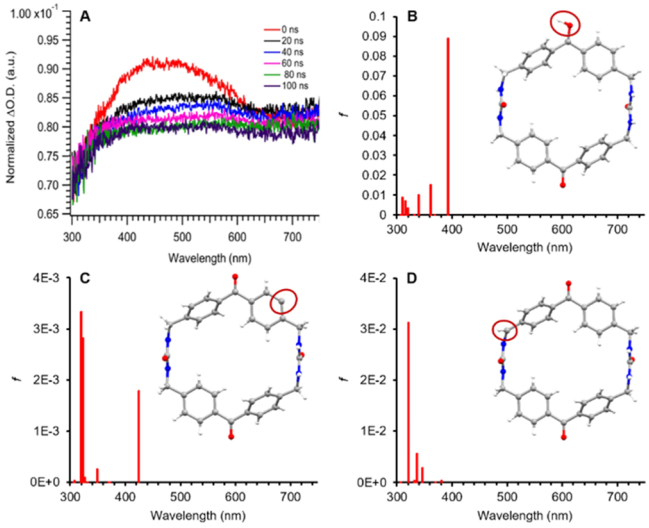

Figure 5. Transient absorption data for argon degassed nanocrystalline suspension of framework **4** (A). Geometry optimized structures and spectral lines from TD-DFT simulations for the ketyl (B), aryl(C), and benzyl(D) radicals of **4** using the ωB97XD/6−31 + G** level of theory. All atoms were frozen at the geometry from the SCXRD data except for those circled in red.

a broad absorption spectrum between 350 and 600 nm, with a maximum absorption at ∼446 nm. The kinetic profile was the same over the spectra and the decay was fitted as mono-exponential decay to yield a lifetime of 78 ns. The lifetime was similar in oxygen saturated solution, but the yields were slightly reduced.

Therefore, LFP shows these three benzophenone frameworks yield transient absorptions that have remarkably similar lifetimes and are presumably formed from a triplet precursor since their yields are affected slightly by oxygen. Thus, we propose that the triplet ketones of **1**, **3** and **4** are short lived as they undergo efficient n-type self-quenching in competition to form these broad transient absorptions. Literature shows that the triplet state of BPs absorption peak overlaps with its corresponding ketyl.[38,39] At this point we cannot rule out whether the persistent radicals are formed from the triplet ketones in competition with self-quenching or from the broad nanosecond transient absorption, or whether they result from the singlet reactivity of the ketone chromophores (Table 1).

Table 1. Solid-State Photophysical Properties of the Urea-Tethered Benzophenone Self-Assembled Frameworks

photophysical properties	1	2	3	4
λ_{max} abs (nm)	366	374[a]	382[a]	355[b]
λ_{max} em (nm)	480	526[a]	528[a]	489[b]
Quantum Efficiency φ (%)	1.55	< 0.3[a]	5.0[a]	< 0.1[c]
Maximum [radical]	70 ± 20 ppm	60 ppm	170 ppm	90 ppm[b]
Radical half-life	5 days	2 days	60 days[a]	>26 days[b]
λ_{max} transient abs (Ar) (nm)	694		688	446
Transient lifetime (Ar) (ns)	70		51	78
Transient lifetime (O_2) (ns)	89		66	60

[a]Values obtained from ref.[9] [b]Values obtained from ref.[7] [c]Values obtained from ref.[21]

https://dx.doi.org/10.1021/acs.jpca.0c08953
J. Phys. Chem. A 2021, 125, 1336−1344

3.5. TD-DFT Simulations of LFP Data. SC-XRD data was used for gas phase geometry optimizations of triplet excited **1**, **3**, and **4** (Figures S15B–S17B). All atoms were space-fixed except for the C═O of the BP closest to abstractable hydrogens. Similarly, geometry optimizations were carried out for each plausible ketyl, aryl, and benzyl radical of **1**, **3**, and **4**, which result from abstraction of proximal hydrogens within 3.13 Å as identified in Figure 4A,C,D. These structures required either the addition of an H for the ketyl radical or H removal for aryl and benzyl radicals. These bond changes define the radical at the abstraction site. For example, Figure 5B shows the ketyl radical of **4**. Optimized geometries were then used in TD-DFT calculations to acquire theoretical spectral lines for comparison with experimental data. All calculations were conducted on a single molecule and the charge was set to 0 with a spin-multiplicity of 3 for the triplet excited species and 2 for each radical. Additionally, geometry optimizations were carried out for a triplet radical pair of **1**, which was used for TD-DFT with a charge set to 0 with a spin multiplicity of 3.

For each species, triplet and radical, the theoretical spectral lines were compared with experimental TA data to identify the most likely species responsible for the transition (Figures S15–S25). Simulations of the transient absorption suggest the longer-lived species could either be triplet excited BP or ketyl or aryl radicals. However, due to the significant deviation in lifetime with the prior studies, triplet excited BP can be ruled out. Computational data for ketyl and aryl radicals from **4** provides a reasonable fit for the experimental TA data (Figure 5) with the strongest transitions at 393 and 425 nm, which roughly correlates with the observed λ_{max} at 446 nm. The benzyl is higher in energy (Figure 5D). In comparison, TD-DFT calculations for the ketyl and aryl radicals for **1** predict that the maximum absorption be at 393 and 417 nm, which do not match the transient absorption well (Figures S18 and S21). In addition, the electronic transitions were calculated for neighboring frozen radical pairs (Figure S25) but were comparable to the single ketyl radical. Similarly, TD-DFT calculations of ketyl and aryl radicals from **3** form predicted maximum absorption at 402 and 411 nm, which are also not a good match with the observed transient at 688 nm. Future work will examine radical pair formation within larger assemblies by TD-DFT. With the LFP data and theoretical simulations indicative of radical pair formation, we turned next to measuring the amount of radicals formed by EPR.

3.6. Quantifying Radical Production by EPR. Previously, we compared the amount of radicals generated upon 1 h UV-irradiation of crystalline **2**–**4**.[7,9] Each structure produced persistent radicals with half-lives ranging from 2 to 60 days, for **2** and **3** respectively, when sealed under argon in quartz EPR tubes (4 mm) and UV-irradiated using a medium pressure Hg arc lamp.[7,9] However, this method can produce quartz impurities in the tube. Thus, further studies employed 365 nm LEDs as they are close to the λ_{max} for **1**–**4** and show a significant reduction in background signal. The power of the LEDs is approximately 30 times less than the Hg lamp (14.4 vs 450 W). The photon flux at 3.5 cm from the LEDs was measured as 9.78×10^{15} photons/sec (Table S16). Experiments conducted herein aim to answer two key questions. Does framework **1** also generate radicals upon UV-exposure? Can **2**–**4** form radicals when irradiated with LEDs in similar or higher quantities as observed using the Hg lamp?

First, triply recrystallized **1** (5.5 mg) was sealed under argon, examined by X-band EPR spectroscopy, and showed very little signal (Figure 6A, black line). The sample was then UV-irradiated for exposures from 1–12 h and radical formation was monitored by EPR. After 1 h, a broad anisotropic signal with a *g*-value of 2.008 was observed. Longer irradiation times showed a similar line shape with an increase in the population of radicals until reaching a plateau after approximately 6–8 h. The quantity of radicals was estimated by double integration of EPR the spectra and comparison to TEMPO standard solutions in benzene (Figure S36). The maximum concentration of radicals in **1** was determined by averaging the last three values from the plateau region and was found to be 1 in 15,000 or 70 ppm, equivalent to 100 μL of a 7.3 μM TEMPO solution.

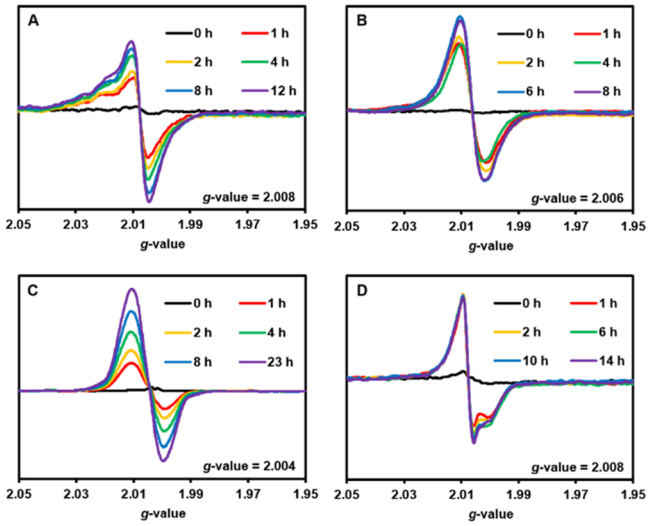

Figure 6. X-band EPR data from the maximum radical generation studies for **1** (A), **2** (B), **3**(C), and **4**(D).

Next, we measured the EPR signal of triply recrystallized **2** (9.4 mg). After irradiation with 365 nm LEDs, the crystals turned yellow with no deformations. After 1 h irradiation, a broad isotropic signal with a g value of 2.006 was observed (Figure 6B). Prior work using the medium pressure Hg lamp showed a second signal, likely generated by a quartz impurity. Double integration gave a measured area equal to a 12 μM TEMPO standard solution, which suggests a radical concentration of 1 in 18,000 molecules or 30 ppm. This radical concentration is lower than the 40 ppm observed upon irradiation (1 h) with the Hg lamp.[9] Increasing exposure of **2** to the LEDs induces more radicals until reaching a plateau after ∼6 h. The maximum radical concentration of **2** under prolonged LED exposure was 1 in 16,000 or 60 ppm as compared to the TEMPO calibration.

The EPR signal of triply recrystallized **3** (10.5 mg) was also measured upon UV-irradiation with 365 nm LEDs. An exposure time of 1 h resulted in pink crystals and the formation of a broad isotropic signal with a g value of 2.004 (Figure 6C). The concentration of radicals was 43 ppm. In comparison, 1 h irradiation with the medium pressure Hg lamp afforded a radical concentration of ∼200 ppm. Again, increasing the time of LED exposure lead to more radicals until reaching a plateau after ∼15 h. The maximum radical concentration of **3** upon exposure to the LEDs was 170 ppm.

https://dx.doi.org/10.1021/acs.jpca.0c08953
J. Phys. Chem. A 2021, 125, 1336–1344

The similarity between the amounts of radical generated by the two light sources of different intensities suggests we are activating similar processes.

Lastly, the EPR signal of triply recrystallized **4** (6.2 mg) was measured upon irradiation with 365 nm LEDs. A 1 h irradiation period resulted in the formation of a broad anisotropic signal with a *g*-value of 2.008 (Figure 6D). The concentration of radicals was 86 ppm, approximately double the amount generated after 1 h irradiation with the Hg lamp (40 ppm).[7] Increased LED exposure times lead to increased radical concentrations until reaching a plateau after 8 h. The maximum radical concentration of **4** upon exposure to the LEDs was 90 ppm.

Figure 7 compares the estimated quantity of radicals generated in **1**−**4** versus irradiation time. Interestingly,

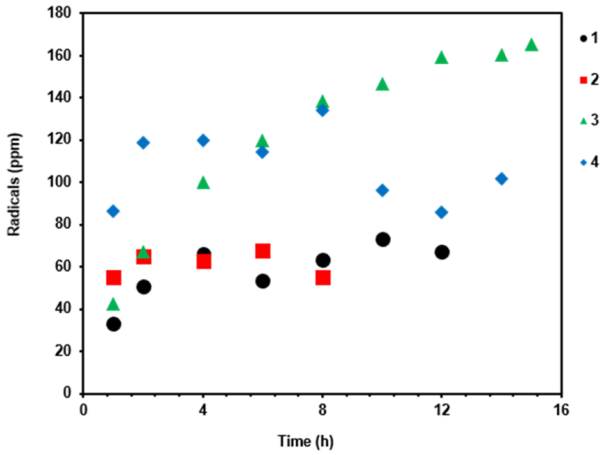

Figure 7. Values from the double integration of each spectra over time of UV irradiation converted to ppm using a TEMPO calibration curve.

frameworks **2** and **4** generate radicals at a noticeably faster rate than **3**. The radical concentration reached a plateau after ∼6 h for **1**, **2**, and **4** whereas **3** required 15 h of UV irradiation (Figure S34). Also notable, **3** generates approximately four times more radicals (∼200 vs 60 ppm) compared to **2**.

For **2**−**4** no degradation was detected by ^{1}H-NMR after maximum radical generation, and the crystals show no changes in SC-XRD.[7,9] Our hypothesis is that radical formation is a reversible process in the solid-state. To compare the radical stability and persistence, the EPR samples of **1** and **2** were UV irradiated until reaching their maximum radical concentration and then placed in the dark. The EPR spectra were recorded periodically and showed no change in line shape but decreased in intensity consistent with a reduction in the amount of radical (Figure 8). The EPR signals were doubly integrated to obtain the area, which was plotted versus time after UV-irradiation. Figure 8B shows the radical concentration of **1** decaying over time with a half-life of ∼5 days. Inspection of Figure 8B suggests there is a faster decay process followed by a longer-lived species. The decay of **2** is shown in Figure 8D also exhibits a steep initial decay from 60 to 20 ppm at ∼100 h with a shorter half-life of ∼2 days. Reported dark decay studies for **3** and **4** suggested significantly longer half-lives of 60 and > 26 days respectively.[7,9]

Usually upon ketyl radical formation in solution, BP reacts to form dimers and the sample must be resynthesized.[13,34] Indeed, irradiation of **2** or **3** in acetonitrile (∼1 mg/mL) for 24

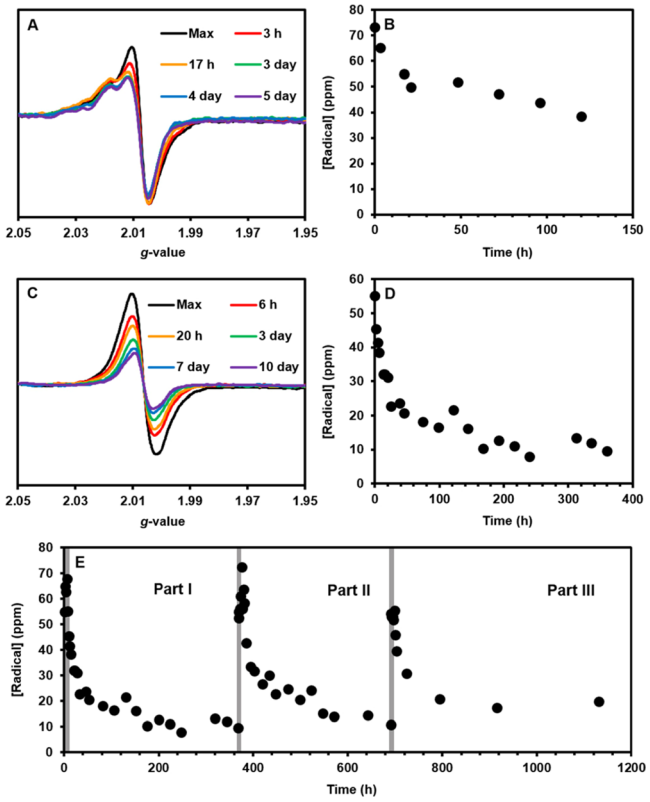

Figure 8. Dark Decay of photoinitiated radicals monitored over time removed from light by X-band EPR of **1** (A) and **2**(C) with corresponding radical concentrations for **1** (B) and **2**(D). Radical concentration values over the course of a radical regeneration study monitored by X-band EPR for **2** (E) whereby exposure times to 365 nm LEDs are highlighted in grey.

h showed loss of all starting material resonances in the ^{1}H NMR (Figures S37−38). In contrast, urea assembly orients the BPs in a geometry that appears to prevent dimerization as no changes were observed by ^{1}H-NMR or X-ray diffraction.[9] Mass spectrometry data for crystalline **2** and **3** also support the robust nature of the urea assemblies (Figure S45−50). Solid-state dynamic nuclear polarization magic angle spinning NMR experiments for compound **4** after 2 h UV irradiation also displayed no signs of degradation.[7]

To test the reusability of our materials and probe for any detectable dimer formation, samples were subjected to three repeated UV irradiation and decay processes. Framework **2** was studied for radical regeneration due to its shorter radical half-life (Figures S31-S33).[40] Once the signal of **2** had decayed after the initial irradiation period to 10 ppm (Figure 8E, Part I), the sample was re-exposed to UV-light. Remarkably, irradiation (14 h) restores the radical concentration to 60 ppm (Figure 8E, Part II). This second decay process exhibits similar kinetics to the first process reaching 10 ppm radical concentration 309 h post irradiation. This sample was then re-irradiated for 10 h, restoring the radical concentration back to its maximum 50 ppm (Figure 8E, Part III). Again, the decay process followed similar kinetics reaching 10 ppm after 337 h. Upon completion of this study, the yellow crystals were dissolved in solvent and checked by ^{1}H-NMR (Figure S40) and positive-ion electrospray mass spectrometry (Figure S45−46). No changes were observed in the ^{1}H-NMR spectra and only slight enhancement of a potential dimer or aggregate peak

https://dx.doi.org/10.1021/acs.jpca.0c08953
J. Phys. Chem. A 2021, 125, 1336−1344

in the mass spectrum was observed suggesting the material is not degraded by these light-activated processes.

4. CONCLUSIONS

Two sets of constitutional isomers, two BP *bis*-urea macrocycles and two methylene-urea tethered dibenzophenones, were crystallized and their self-assembly motifs were elucidated with SC-XRD. Photophysical studies along with LFP measurements on crystalline **1**−**4** suggest that the photodriven process primarily occurs through typical BP ISC from $S_1 \rightarrow T_2 \rightarrow T_1$, with phosphorescence and non-radiative emission making up the major pathways and formation of a broad transient absorption. Upon UV-irradiation using 365 nm LEDs, assembled **1**−**4** generated persistent radicals, whereas no radicals were observed in solution. EPR studies demonstrated that longer irradiation times induced increased radical formation until reaching a plateau, with maximum radical concentrations that differed depending on the structure, from 60 ∼90 ppm for **1**, **2** and **4** up to ∼200 ppm for **3**. Upon storage in the dark, the amount of radicals decreased without formation of new products or dimers. This suggests that radical formation may be limited by the competing processes for ex. self-quenching, non-radiative decay, phosphorescence, etc., rather than by the rate of the reverse radical process. The assembled linear analog **2** possessed the shortest half-life of its photogenerated radicals and was therefore chosen for a radical regeneration study. Reirradiation of assembled **2** after initial decay formed radicals in similar quantities, demonstrating their regenerability. Three cycles of radical generation and subsequent decay were followed on a single sample. Characterization of the sample after the final decay did not display degradation by ^{1}H-NMR or mass spectroscopy, suggesting that any radicals formed recombined or underwent reverse processes to reform the starting material.

Structural analysis, including distances (R), azimuth (Θ) angles, and altitude (Φ) angles between BP oxygen and centroids of the two nearest aryl rings, reveals all four materials are suitable for n-type self-quenching. Consistent with n-type self-quenching all four assemblies have a low phosphorescence quantum efficiency with values ranging from <0.1 to 5.0%. The material capable of generating the most radicals, **3**, also possesses the highest phosphorescence quantum efficiency. These two measurements give evidence to suggest assembled **3** is the least efficient material at n-type self-quenching. Interestingly, the geometry of **3** displays the best theoretical altitude (Φ) angles of all materials in the series but does not have azimuth (Θ) angles within the ideal range. Therefore, possessing the correct azimuth angle seems a higher priority than optimizing the altitude angle for n-type self-quenching to occur. This finding should be considered when designing future hierarchical materials that necessitate close proximity of chromophores where self-quenching is undesirable.

ASSOCIATED CONTENT

Supporting Information

The Supporting Information is available free of charge at https://pubs.acs.org/doi/10.1021/acs.jpca.0c08953.

Product characterization, X-ray, photophysical characterization, NMR, EPR, LFP, TD-DFT, and mass spectrometry (PDF).

X-ray data for **1** (CIF)

AUTHOR INFORMATION

Corresponding Author

Linda S. Shimizu − *Department of Chemistry and Biochemistry, University of South Carolina, Columbia, South Carolina 29208, United States*; Email: shimizls@mailbox.sc.edu

Authors

Dustin W. Goodlett − *Department of Chemistry and Biochemistry, University of South Carolina, Columbia, South Carolina 29208, United States*

Ammon J. Sindt − *Department of Chemistry and Biochemistry, University of South Carolina, Columbia, South Carolina 29208, United States*

Muhammad Saddam Hossain − *Department of Chemistry and Biochemistry, University of South Carolina, Columbia, South Carolina 29208, United States*

Rajkumar Merugu − *Department of Chemistry, University of Cincinnati, Cincinnati, Ohio 45221, United States*

Mark D. Smith − *Department of Chemistry and Biochemistry, University of South Carolina, Columbia, South Carolina 29208, United States*

Sophya Garashchuk − *Department of Chemistry and Biochemistry, University of South Carolina, Columbia, South Carolina 29208, United States*; orcid.org/0000-0003-2452-7379

Anna D. Gudmundsdottir − *Department of Chemistry, University of Cincinnati, Cincinnati, Ohio 45221, United States*; orcid.org/0000-0002-5420-4098

Complete contact information is available at: https://pubs.acs.org/10.1021/acs.jpca.0c08953

Notes

The authors declare no competing financial interest.

ACKNOWLEDGMENTS

This work was supported in part by the National Science Foundation CHE-1904386, CHE-1955768, CHE-1800140, and OIA-1655740.

REFERENCES

(1) Wang, P.; Miao, X.; Meng, Y.; Wang, Q.; Wang, J.; Duan, H.; Li, Y.; Li, C.; Liu, J.; Cao, L. Tetraphenylethene-Based Supramolecular Coordination Frameworks with Aggregation-Induced Emission for an Artificial Light-Harvesting System. *ACS Appl. Mater. Interfaces* **2020**, *12*, 22630−22639.

(2) Albino De Souza, G.; De Castro Bezerra, F.; Martins, T. D. Photophysical Properties of Fluorescent Self-Assembled Peptide Nanostructures for Singlet Oxygen Generation. *ACS Omega* **2020**, *5*, 8804−8815.

(3) Pang, P.; Miao, X.; Ying, L.; Kong, G.; Che, C.; Deng, W. Halogen-Bond-Controlled Self-Assembly of Regioisomeric Phenanthridine Derivatives into Nanowires and Nanosheets. *J. Phys. Chem. C* **2020**, *124*, 5665−5671.

(4) Kittikhunnatham, P.; Som, B.; Rassolov, V.; Stolte, M.; Würthner, F.; Shimizu, L. S.; Greytak, A. B. Fluorescence Polarization Measurements to Probe Alignment of a Bithiophene Dye in One-Dimensional Channels of Self-Assembled Phenylethynylene Bis-Urea Macrocycle Crystals. *J. Phys. Chem. C* **2017**, *121*, 18102−18109.

(5) Sindt, A. J.; Smith, M. D.; Berens, S.; Vasenkov, S.; Bowers, C. R.; Shimizu, L. S. Single-Crystal-to-Single-Crystal Guest Exchange in Columnar Assembled Brominated Triphenylamine Bis-Urea Macrocycles. *Chem. Commun.* **2019**, *55*, 5619−5622.

(6) Dehaven, B. A.; Liberatore, H. K.; Greer, A.; Richardson, S. D.; Shimizu, L. S. Probing the Formation of Reactive Oxygen Species by a Porous Self-Assembled Benzophenone Bis-Urea Host. *ACS Omega* **2019**, *4*, 8290−8298.
(7) DeHaven, B. A.; Tokarski, J. T.; Korous, A. A.; Mentink-Vigier, F.; Makris, T. M.; Brugh, A. M.; Forbes, M. D. E.; van Tol, J.; Bowers, C. R.; Shimizu, L. S. Persistent Radicals of Self-Assembled Benzophenone *Bis*-Urea Macrocycles: Characterization and Application as a Polarizing Agent for Solid-State DNP MAS Spectroscopy. *Chem. − Eur. J.* **2017**, *23*, 8315−8319.
(8) Sindt, A. J.; Dehaven, B. A.; McEachern, D. F.; Dissanayake, D. M. M. M.; Smith, M. D.; Vannucci, A. K.; Shimizu, L. S. UV-Irradiation of Self-Assembled Triphenylamines Affords Persistent and Regenerable Radicals. *Chem. Sci.* **2019**, *10*, 2670−2677.
(9) Dehaven, B. A.; Goodlett, D. W.; Sindt, A. J.; Noll, N.; De Vetta, M.; Smith, M. D.; Martin, C. R.; González, L.; Shimizu, L. S. Enhancing the Stability of Photogenerated Benzophenone Triplet Radical Pairs through Supramolecular Assembly. *J. Am. Chem. Soc.* **2018**, *140*, 13064−13070.
(10) Sergentu, D.-C.; Maurice, R.; Havenith, R. W. A.; Broer, R.; Roca-Sanjuá, D. Computational Determination of the Dominant Triplet Population Mechanism in Photoexcited Benzophenone †. *Phys. Chem. Chem. Phys.* **2014**, *16*, 25393−25403.
(11) Kreiza, G.; Banevič, D.; Jovaišaite, J.; Maleckaite, K.; Gudeika, D.; Volyniuk, D.; Gražulevičius, J. V.; Juršenas, S.; Kazlauskas, K. Suppression of Benzophenone-Induced Triplet Quenching for Enhanced TADF Performance. *J. Mater. Chem. C* **2019**, *7*, 11522−11531.
(12) Scott, T. A.; Ooro, B. A.; Collins, D. J.; Shatruk, M.; Yakovenko, A.; Dunbar, K. R.; Zhou, H.-C. After 118 years, the Isolation of Two Common Radical Anion Reductants as Simple. *Chem. Commun.* **2009**, 65−67.
(13) Adjibodéa, S. M.; Kasséhin, U. C.; Gbaguidi, F. A.; Poupaert, J. H. Synthesis of Icosadeuterio-Benzopinacol (Benzopinacol-D20). *J. Med. Chem. Sci.* **2020**, *3*, 35−40.
(14) Iwakura, Y.; Takeda, K.; Nakazawa, T.; Watarai, O. Trapping of Benzophenone Ketyl Radical in Cellulose Triacetate Film. *J. Polym. Sci. B Polym. Lett.* **1968**, *6*, 115−118.
(15) Terenin, A.; Ermolaev, V. Sensitized Phosphorescence in Organic Solutions at Low Temperature: Energy Transfer Between Triplet States. *Trans. Faraday Soc.* **1956**, *52*, 1042−1052.
(16) Wolf, M. W.; Legg, K. D.; Brown, R. E.; Singer, L. A.; Parks, J. H. Photophysical Studies on the Benzophenones. Prompt and Delayed Fluorescences and Self-Quenching. *J. Am. Chem. Soc.* **1975**, *97*, 4490−4497.
(17) Kuzmanich, G.; Simoncelli, S.; Gard, M. N.; Spanig, F.; Henderson, B. L.; Guldi, D. M.; Garcia-Garibay, M. A. Excited State Kinetics in Crystalline Solids: Self-Quenching in Nanocrystals of 4,4'-Disubstituted Benzophenone Triplets Occurs by a Reductive Quenching Mechanism. *J. Am. Chem. Soc.* **2011**, *133*, 17296−17306.
(18) Schmidt, G. M. J. Photodimerization in the Solid State. *Pure Appl. Chem.* **1971**, *27*, 647−678.
(19) Gudmundsdottir, A. D.; Lewis, T. J.; Randall, L. H.; Scheffer, J. R.; Rettig, S. J.; Trotter, J.; Wu, C. H. Geometric Requirements for Hydrogen Abstractability and 1,4-Biradical Reactivity in the Norrish/Yang Type II Reaction: Studies Based on the Solid State Photochemistry and X-Ray Crystallography of Medium-Sized Ring and Macrocyclic Diketones. *J. Am. Chem. Soc.* **1996**, *118*, 6167−6184.
(20) Dewal, M. B.; Xu, Y.; Yang, J.; Mohammed, F.; Smith, M. D.; Shimizu, L. S. Manipulating the Cavity of a Porous Material Changes the Photoreactivity of Included Guests. *Chem. Commun.* **2008**, 3909−3911.
(21) Geer, M. F.; Walla, M. D.; Solntsev, K. M.; Strassert, C. A.; Shimizu, L. S. Self-Assembled Benzophenone Bis-Urea Macrocycles Facilitate Selective Oxidations by Singlet Oxygen. *J. Org. Chem.* **2013**, *78*, 5568−5578.
(22) *APEX3 Version 2018.1−0 and SAINT+ Version 8.38A*. Bruker AXS, Inc., Madison, Wisconsin, USA, 2016.
(23) Krause, L.; Herbst-Irmer, R.; Sheldrick, G. M.; Stalke, D. Comparison of Silver and Molybdenum Microfocus X-Ray Sources for Single-Crystal Structure Determination. *J. Appl. Crystallogr.* **2015**, *48*, 3−10.
(24) Sheldrick, G. M. SHELXT − Integrated Space-Group and Crystal-Structure Determination. *Acta Crystallogr., Sect. A: Found. Adv.* **2015**, *A71*, 3−8.
(25) Sheldrick, G. M. Crystal Structure Refinement with SHELXL. *Acta Crystallogr. Sect. C Struct. Chem.* **2015**, *71*, 3−8.
(26) Dolomanov, O. V.; Bourhis, L. J.; Gildea, R. J.; Howard, J. A. K.; Puschmann, H. OLEX2: A Complete Structure Solution, Refinement and Analysis Program. *J. Appl. Crystallogr.* **2009**, *42*, 339−341.
(27) Sarkar, S. K.; Ranaweera, R. A. A. U.; Merugu, R.; Abdelaziz, N. M.; Robinson, J.; Day, H. A.; Krause, J. A.; Gudmundsdottir, A. D. Comparison of the Photochemistry of Acyclic and Cyclic 4-(4-Methoxy-Phenyl)-4-Oxo-but-2-Enoate Ester Derivatives. *J. Phys. Chem. A* **2020**, *124*, 7346−7354.
(28) Mennucci, B. Polarizable Continuum Model. *WIREs Comput. Mol. Sci.* **2012**, *2*, 386−404.
(29) Shao, Y.; Gan, Z.; Epifanovsky, E.; Gilbert, A. T. B.; Wormit, M.; Kussmann, J.; Lange, A. W.; Behn, A.; Deng, J.; Feng, X.; et al. Advances in Molecular Quantum Chemistry Contained in the Q-Chem 4 Program Package. *Mol. Phys.* **2015**, *113*, 184−215.
(30) Plasser, F.; Bappler, S. A.; Wormit, M.; Dreuw, A. New Tools for the Systematic Analysis and Visualization of Electronic Excitations. II Application. *J. Chem Phys.* **2014**, *141*, No. 024107.
(31) Campbell, J. E.; Yang, J.; Day, G. M. Predicted Energy-Structure-Function Maps for the Evaluation of Small Molecule Organic Semiconductors. *J. Mater. Chem. C* **2017**, *5*, 7574−7584.
(32) Marchetti, B.; Karsili, T. N. V.; Ashfold, M. N. R. Exploring Norrish Type I and Type II Reactions: An Ab Initio Mechanistic Study Highlighting Singlet-State Mediated Chemistry. *Phys. Chem. Chem. Phys.* **2019**, *21*, 14418−14428.
(33) McMillen, D. F.; Golden, D. M. Hydrocarbon Bond Dissociation Energies. *Annu. Rev. Phys. Chem.* **1982**, *33*, 493−532.
(34) Ito, Y.; Matsuura, T.; Tabata, K.; Ji-Ben, M.; Fukuyama, K.; Sasaki, M.; Okada, S. Solid State Photochemistry of Methyl-Substituted Benzophenones. *Tetrahedron* **1987**, *43*, 1307−1312.
(35) Hideko, K.; Hessler Bittl, D. P.; Fumihiro, M.; Yang, W.; Teruo, M. Photochemical Hydrogen Abstraction by Benzophenones from Hydrogen Donors in the Solid State. *J. Photochem. Photobiol., A* **1995**, *86*, 171−176.
(36) St John, P.; Guan, Y.; Kim, Y.; Kim, S.; Paton, R. S. Prediction of Homolytic Bond Dissociation Enthalpies for Organic Molecules at near Chemical Accuracy with Sub-Second Computational Cost. *ChemRxiv* **2019**, *11*, 2328.
(37) Buettner, A. V.; Dedinas, J. Photoreduction of Benzophenone in Benzene. II. Flash Photolysis Study of Primary Photochemical Reactions. *J. Phys. Chem.* **1971**, *75*, 187−191.
(38) Encinas, M. V.; Scaiano, J. C. Reaction of Benzophenone Triplets with Allylic Hydrogens. A Laser Flash Photolysis Study. *J. Am. Chem. Soc.* **1981**, *103*, 6393−6397.
(39) Turro, N. J.; Ramamurthy, V.; Scaiano, J. C. *Modern Molecular Photochemistry of Organic Molecules;* University Science Books: Sausalito, CA, 2010; 483−624.
(40) Sindt, A. J.; Dehaven, B. A.; Goodlett, D. W.; Hartel, J. O.; Ayare, P. J.; Du, Y.; Smith, M. D.; Mehta, A. K.; Brugh, A. M.; Forbes, M. D. E.; et al. Guest Inclusion Modulates Concentration and Persistence of Photogenerated Radicals in Assembled Triphenylamine Macrocycles. *J. Am. Chem. Soc.* **2020**, *142*, 502−511.

https://dx.doi.org/10.1021/acs.jpca.0c08953
J. Phys. Chem. A 2021, 125, 1336−1344